GAS-SURFACE IMPACT ON SHOCK WAVE STRUCTURE OF LOW-DENSITY HYPERSONIC FLOW OVER FLAT-NOSE BODIES

Wilson F. N. Santos
National Institute for Space Research
Combustion and Propulsion Laboratory
12630-000 Cachoeira Paulista, SP, Brazil
wilson@lcp.inpe.br

Abstract. *Computations using the Direct Simulation Monte Carlo (DSMC) method are presented for rarefied hypersonic flow over flat-nose leading edges. The primary aim of this paper is to examine the effects of partial surface accommodation on the shock wave structure. Partial surface accommodation effects on the shock wave structure have been investigated by employing the DSMC method in combination with the Cercignani-Lampis-Lord gas-surface interaction model, which incorporates separate accommodation coefficients for normal and tangential velocity components. The sensitivity of shock wave shape, shock standoff distance, and shock thickness is calculated by using a model that classifies the molecules in three distinct classes, i.e., "undisturbed freestream", "reflected from the boundary" and "scattered", i.e., molecules that had been indirectly affected by the presence of the leading edge. The analysis shows significant differences on the shock wave structure due to variations on the normal and tangential accommodation coefficients.*

Keywords: *DSMC, hypersonic flow, rarefied flow, blunt leading edge, shock standoff distance.*

1. Introduction

In typical aerospace missions, vehicle performance is directly related to the aerodynamic characteristics of the design. In particular, the lift-drag (L/D) ratio indicates one aspect of the aerodynamic efficiency of the vehicle. One class of aerospace vehicles that have shown the ability to attain a higher L/D ratio compared to the conventional designs is waveriders. Waveriders are designed analytically with infinitely sharp leading edges for shock wave attachment. The potential for high L/D ratio on waveriders originates from the high-pressure region between the shock wave and the lower surface. Due to the sharp leading edge, the attached shock wave prevents the high-pressure gas from the lower surface to communicate with the gas on the upper surface. However, as any practical waverider will have some degree of leading edge bluntness for heat transfer, manufacturing and handling concerns, then the predicted performance of waverider configurations may not be achieved. Moreover, because of the viscous effects, the shock wave will be detached from the leading edge and, hence, the aerodynamic performance of the vehicle may be degraded from ideal performance. Typically, a round leading edge (circular cylinder) with constant radius of curvature near the stagnation point has been chosen. Nevertheless, shock detachment distance on a cylinder, with associated leakage, scales with the radius of curvature. Certain classes of non-circular shapes may provide the required bluntness with smaller shock separation than round leading edges, thus allowing manufacturing, and ultimately heating control, with reduced aerodynamic losses.

In this connection, a typical blunt body, composed of a flat nose followed by a highly curved, but for the most part slightly inclined afterbody surface, may provide the required bluntness for heat transfer, manufacturing and handling concerns with reduced departures from ideal aerodynamic performance. This concept is based on work of Reller (1957), who has pointed out that this shape results from a method of designing low heat transfer bodies. According to Reller (1957), low heat transfer bodies is devised on the premise that the rate of heat transfer to the nose will be low if the local velocity is low, while the rate of heat transfer to the afterbody will be low if the local density is low.

A great deal of works (Santos, 2003, 2004, and 2005) has been carried out recently on flat-nose form representing blunt geometries. The major interest in these works has gone into considering the flat-nose shape as possible candidate for blunting geometries of hypersonic leading edges. Based on recent interest in hypersonic waveriders for high-altitude/low-density applications (Shvets et al., 2005), Santos (2004) has investigated the effect of the leading edge thickness on the shock wave structure over these flat-nose leading edges. Nevertheless, that work (Santos, 2004) has been concentrated primarily on the analysis of the flowfield structure by considering the diffuse reflection model as being the gas-surface interaction. Nonetheless, as a space flight vehicle is exposed to a rarefied environment over a considerable time, a departure from fully diffuse model is observed, resulting from the colliding molecules that clean the surface of the vehicle, which becomes gradually decontaminated. The flux distribution of scattered molecules emitted from clean surfaces frequently has a lobular shape that is centered about an angle that tends to approach the specular angle for very high energies and/or low angle of attack.

In this scenario, the emphasis of this work is to assess the sensitivity of the shock standoff distance, shock wave thickness and shock wave shape to variations on surface accommodation coefficient. For the high altitude/high Knudsen number of interest ($Kn > 0.1$), the flowfield is sufficiently rarefied that continuum method becomes inappropriate. Alternatively, the DSMC method is used in the current study to calculate the rarefied hypersonic two-dimensional flow on the leading edge shapes.

2. Leading Edge Geometry

In dimensionless form, the contour that defines the shape of the afterbody surface is given by the following expression,

$$\bar{x} = \int_{\bar{y}=1}^{\bar{y}=\bar{y}_{max}} \sqrt{\bar{y}^k - 1}\, d\bar{y} \qquad \text{where } \bar{x} = x/y_{nose} \text{ and } \bar{y} = y/y_{nose} \tag{1}$$

The flat-nose shapes are modeled by assuming a sharp leading edge of half angle θ with a circular cylinder of radius R inscribed tangent to the wedge. The flat-nose shapes, inscribed between the wedge and the cylinder, are also tangent to them at the same common point where they have the same slope angle. The circular cylinder diameter provides a reference for the amount of blunting desired on the leading edges. It was assumed a leading edge half angle of 10 deg, a circular cylinder diameter of 10^{-2} m and flat-nose thickness t/λ_∞ of 0.01, 0.1 and 1, where $t = 2y_{nose}$ and λ_∞ is the freestream mean free path. Figure 1(a) illustrates this construction for the set of shapes investigated. From geometric considerations, the exponent k in Eq. (1) is obtained by matching slope on the wedge, circular cylinder and on the body shapes at the tangency point. For dimensionless thickness t/λ_∞ of 0.01, 0.1 and 1, k corresponds to 0.501, 0.746 and 1.465, respectively. The common body height H and the body length L are obtained in a straightforward manner.
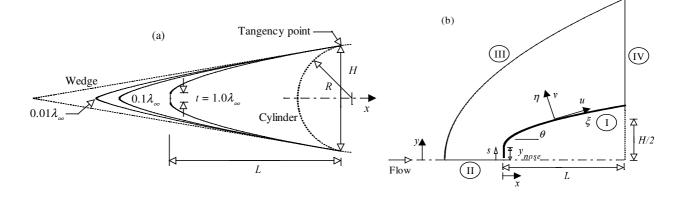

Figure 1: Drawing illustrating (a) the leading edge shapes and (b) the computational domain.

3. Computational Tool

In this study, the particle simulations were performed by using the DSMC method developed by Bird (1994). The DSMC method simulates fluid flow by using thousands to millions of particles. These particles are tracked as they move, collide and undergo boundary interactions in simulated physical space. In addition, particle motions are assumed to be decoupled from particle collisions and each process is computed independently during a time step used to advance the simulation. This time step must be sufficiently small in comparison with the local mean collision time (Bird, 1994) such that the assumption of decoupled particle motions and collisions is not violated.

The molecular collisions are modeled using the variable hard sphere (VHS) molecular model (Bird, 1981) and the no time counter (NTC) collision sampling technique (Bird, 1989). The energy exchange between kinetic and internal modes is controlled by the Borgnakke-Larsen statistical model (Borgnakke and Larsen, 1975). Simulations are performed using a non-reacting gas model consisting of two chemical species, N_2 and O_2. Energy exchanges between the translational and internal modes are considered. For this study, the relaxation numbers of 5 and 50 were used for the rotation and vibration, respectively.

4. Computational Flow Domain and Grid

The computational domain is made large enough so that the upstream and side boundaries can be specified as freestream conditions. Figure 1(b) depicts the physical extent of the computational domain for the present simulations. Advantage of the flow symmetry is taken into account, and molecular simulation is applied to one-half of a full configuration. The computational domain is divided into an arbitrary number of regions, which are subdivided into computational cells. The cells are further subdivided into four subcells, two subcells/cell in each coordinate direction. The linear dimensions of the cells should be small in comparison with the scale length of the macroscopic flow gradients normal to the streamwise directions, which means that the cell dimensions should be of the order of or even smaller than the local mean free path (Bird, 1994). In the current DSMC code, the cell provides a convenient reference

for the sampling of the macroscopic gas properties, while the collision partners are selected from the same subcell. As a result, the flow resolution is much higher than the cell resolution.

Referring to Fig. 2(b), side I is defined by the body surface. Reflection with incomplete surface accommodation is the condition applied to this side. Side II is a plane of symmetry, where all flow gradients normal to the plane are zero. At the molecular level, this plane is equivalent to a specular reflecting boundary. Side III is the freestream side through which simulated molecules enter and exit. Finally, the flow at the downstream outflow boundary, side IV, is predominantly supersonic and vacuum condition is specified (Bird, 1994). At this boundary, simulated molecules can only exit.

Numerical accuracy in DSMC method depends on the grid resolution chosen as well as the number of particles per computational cell. Both effects were investigated to determine the number of cells and the number of particles required to achieve grid independence solutions. Grid independence was tested by running the calculations with half and double the number of cells in ξ and η directions (see Fig. 1(b)) compared to a standard grid. The sensitivity of the surface to grid resolution was obtained for skin friction, heat transfer rate and pressure. Solutions (not shown) were near identical for all grids used and were considered fully grid independent.

5. Freestream and Flow Conditions

The freestream and flow conditions used in the present calculations are those given by Santos (2003) and summarized in Tab. 1. The freestream velocity V_∞, assumed to be constant at 3.56 km/s, corresponds to a freestream Mach number M_∞ of 12. The wall temperature T_w is assumed constant at 880 K, which corresponds to four times the freestream temperature.

Table 1: Freestream Conditions

Temperature T_∞ (K)	Pressure p_∞ (N/m^2)	Density ρ_∞ (kg/m^3)	Number density n_∞ (m^{-3})	Viscosity μ_∞ (Ns/m^2)	Mean free path λ_∞ (m)	Velocity V_∞ (m/s)
220.0	5.582	8.753 x 10^{-5}	1.8209 x 10^{21}	1.455 x 10^{-5}	9.03 x 10^{-4}	3560

The overall Knudsen number Kn_t, defined as the ratio of the freestream mean free path λ_∞ to the leading edge thickness t, corresponds to 1, 10 and 100 for leading edge thickness t/λ_∞ of 1, 0.1 and 0.01, respectively. The Reynolds number Re_t covers the range from 0.193 to 19.3, based on conditions in the undisturbed stream with leading edge thickness t as the characteristic length.

In order to simulate the partial surface accommodation, the Cercignani-Lampis-Lord (CLL) model (Lord, 1991) was implemented into this DSMC calculation. The CLL model is derived assuming that there is no coupling between the normal and tangential momentum components. The two adjustable parameters appearing in the CLL model are the normal component of translational energy α_n and the tangential component of momentum σ_t. In this work, the DSMC calculations were performed independently for three distinct numerical values for α_n and σ_t: 0.5, 0.75 and 1. It is important to mention that α_n and σ_t equal to 1 represent the diffusion reflection.

6. Computational Procedure

In a rarefied flow, the shock wave has a finite region that depends on the transport properties of the gas, and can no longer be considered as a discontinuity obeying the classical Rankine-Hugoniot relations. In this context, the shock wave structure, defined by shape, thickness and detachment of the shock wave, is predicted by employing a procedure based on the physics of the particles. In this respect, the flow is assumed to consist of three distinct classes of molecules; class I molecules denote those molecules from the freestream that have not been affected by the presence of the leading edge; class II molecules designate those molecules that, at some time in their past history, have struck and been reflected from the body surface; and finally, class III molecules define those molecules that have been indirectly affected by the presence of the body. Figure 2(a) illustrates the definition for the molecular classes.

It is assumed that the class I molecule changes to class III molecule when it collides with class II or class III molecule. Class I or class III molecule is progressively transformed into class II molecule when it interacts with the body surface. Also, a class II molecule remains class II regardless of subsequent collisions and interactions. Hence, the transition from class I molecules to class III molecules may represent the shock wave, and the transition from class III to class II may define the boundary layer.

A typical distribution of class III molecules along the stagnation streamline for blunt leading edges is displayed in Fig. 2(b) along with the definition used to determine the thickness, displacement and shape of the shock wave. In this figure, X is the distance x along the stagnation streamline (see Fig. 1(b)), normalized by the freestream mean free path λ_∞ and f_{III} is the number of molecules for class III to the total amount of molecules inside each cell.

The shock standoff distance Δ is defined as being the distance between the shock wave center and the nose of the

leading edge along the stagnation streamline. As shown in Fig. 2(b), the center of the shock wave is defined by the station that corresponds to the maximum value for f_{III}. The shock wave thickness δ is defined by the distance between the stations that corresponds to the mean value for f_{III}. Finally, the shock wave shape (shock wave "location") is determined by the coordinate points given by the maximum value in the f_{III} distribution along the lines departing from the body surface, i.e., η-direction as shown in Fig. 1(b).
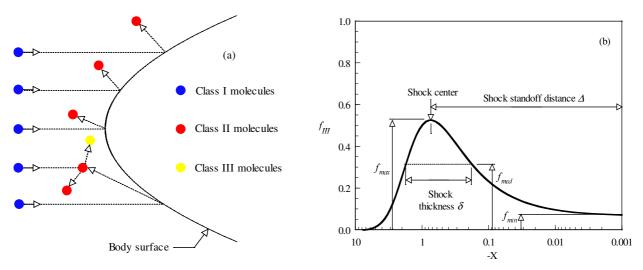

Figure 2: (a) Drawing illustrating the classification of molecules and (b) schematic of shock wave structure.

7. Computational Results and Discussion

The purpose of this section is to discuss and to compare differences in the shape, thickness and displacement of the shock wave due to variations on the surface accommodation coefficients as well as on the leading edge thickness.

The distribution of molecules for the three classes along the stagnation streamline is illustrated in Fig. 3 for nose thickness corresponding to Kn_t of 100 (t/λ_∞ of 0.01). Figure 3(a) displays the distribution of molecules for normal accommodation coefficient α_n of 0.5 and 1 and Fig. 3(b) for the tangential accommodation coefficient σ_t of 0.5 and 1. It is important to note that $\alpha_n = \sigma_t = 1$ represent the diffuse reflection case. In addition, in this set of plots, f_I, f_{II} and f_{III} are the ratio of the number of molecules for class I, II and III, respectively, to the total amount of molecules inside each cell along the stagnation streamline. By examining Fig. 3, it is clearly seen that partial accommodation coefficient affects the shock wave structure for this particular sharp leading edge. Consequently, changes in the normal and tangential accommodation coefficients will affect the shape, thickness and displacement of the shock wave in a different manner.

Figure 4 shows the distribution of molecules for the three classes along the stagnation streamline for nose thickness corresponding to Kn_t of 1 (t/λ_∞ of 1). Similarly, Fig. 4(a) illustrates the distribution of molecules for normal accommodation coefficient α_n of 0.5 and 1 and Fig. 4(b) for the tangential accommodation coefficient σ_t of 0.5 and 1.
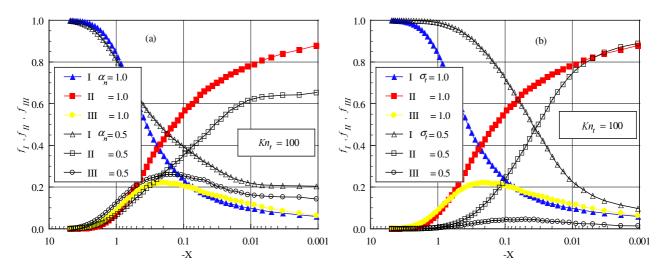

Figure 3: Distributions of molecules for classes I, II and III along the stagnation streamline for the leading edge case that correspond to thickness Knudsen number Kn_t of 100 and (a) α_n of 0.5 and (b) σ_t of 0.5.
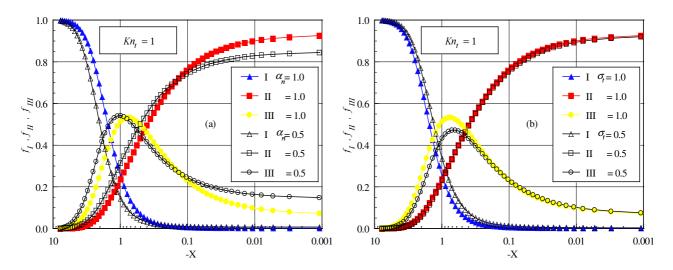
Figure 4: Distributions of molecules for classes I, II and III along the stagnation streamline for the leading edge case that correspond to thickness Knudsen number Kn_t of 1 and (a) α_n of 0.5 and (b) σ_t of 0.5.

It is noted from this set of plots that normal and tangential accommodation coefficients have little effect on the shock wave structure along the stagnation streamline provided the leading edge is blunt.

Of great significance in the plots shown in Figs. 3 and 4 is the behavior of the class I molecules for sharp and blunt leading edges. It should be observed that molecules from freestream, represented by class I molecules, collide with the nose of the leading edges even after the establishment of the steady state. This is shown in Fig. 3, which represent sharp leading edge cases. In contrast, molecules from freestream do not reach the nose of the leading edge for those cases illustrated in Fig. 4, that represent blunt leading edge. This is explained by the fact that density (Santos, 2003) increases much more for blunt (flat) leading edges in the stagnation region and reaches its maximum value in the stagnation point. In this connection, the buildup of particle density near the nose of the leading edge acts as a shield for the molecules coming from the undisturbed stream. The class distributions for the other cases investigated in this work are intermediate to these four cases and, therefore, they will not be shown.

7.1. Shock Wave Standoff Distance

According to the definition shown in Fig. 2(b), the shock wave standoff distance Δ can be observed in Figs. 3 and 4 for the flat-nose shapes shown. The calculated shock wave standoff distance Δ, normalized by the freestream mean free path λ_∞, is tabulated in Tab. 2 for the cases investigated. It is apparent from these results that there is a discrete shock standoff distance for the cases shown. As would be expected, the shock standoff distance increases with increasing the flat-nose thickness. It is also seen that, in general, the shock standoff distance decreases with decreasing the tangential accommodation coefficient and increases by a reduction in the normal accommodation coefficient, even though the shock standoff distance decreased slightly for the sharpest leading edge, Kn_t of 100, as the normal accommodation coefficient changed from 1 to 0.5.

Table 2: Dimensionless shock wave standoff distance Δ/λ_∞ for flat-nose leading edges.

	$Kn_t = 100$	$Kn_t = 10$	$Kn_t = 1$
Diffuse	0.201	0.346	0.753
$\alpha_n = 0.75$	0.157	0.421	0.867
$\alpha_n = 0.50$	0.151	0.459	1.008
$\sigma_t = 0.75$	0.107	0.265	0.696
$\sigma_t = 0.50$	0.049	0.212	0.656

For comparison purpose, the circular cylinder, shown in Fig. 1(a), provides a larger shock detachment, i.e., Δ/λ_∞ of 1.65, 1.81 and 1.54 for diffuse, $\alpha_n = 0.5$ and $\sigma_t = 0.5$, respectively, according to Santos (2005). These values are about 2.2, 1.8 and 2.3 times larger than those to Kn_t of 1, respectively. The results tend to confirm the expectation that the shock standoff distance for sharp leading edge is smaller than that for blunt leading edge. In fact, the flat-nose bodies behave as if they had a sharper profile than the representative circular cylinder.

It is important to mention that shock standoff distance becomes important in hypersonic vehicles such as waveriders, which depend on leading edge shock attachment to achieve their high lift-to-drag ratio at high lift coefficient. In this

connection, the flat-nose shapes seem to be more appropriate than the circular cylinder, since they present reduced shock wave detachment distances. Nonetheless, smaller shock detachment distance is associated with a higher heat load to the nose of the body. According to Santos (2003), the heat transfer coefficient C_{ho} (= $2q_w/\rho_\infty V_\infty^3$) at the stagnation point for flat-nose bodies, Kn_t of 100, 10 and 1 are 2.4, 2.2 and 1.5 times larger than that for the circular cylinder by considering diffuse case. As a result, it should be notice from this comparison that the ideal blunting leading edge depends on the context. If shock standoff distance is the primary issue in leading edge design of hypersonic waveriders, then flat-nose leading edges are superior to round leading edges. Contrary, if the stagnation point heating is the important parameter in the hypersonic vehicle design, then round shapes seem to be superior to the flat-nose shapes.

7.2. Shock Wave Thickness

Based on the definition of the shock wave thickness shown in Fig. 2(b), the shock wave thickness δ along the stagnation streamline can be obtained from Figs. 3 and 4 for the flat-nose shapes. As a result of the calculation, Tab. 3 tabulates the shock wave thickness δ, normalized by the freestream mean free path λ_∞, for the cases investigated.

Table 3: Dimensionless shock wave thickness δ/λ_∞ for flat-nose leading edges.

	$Kn_t = 100$	$Kn_t = 10$	$Kn_t = 1$
Diffuse	0.652	0.864	1.673
$\alpha_n = 0.75$	0.550	0.917	1.783
$\alpha_n = 0.50$	0.503	0.953	1.947
$\sigma_t = 0.75$	0.369	0.662	1.568
$\sigma_t = 0.50$	0.248	0.531	1.488

It is evident from Tab. 3 that the shock wave thickness follows the same trend presented by the shock wave standoff distance in that it decreases with decreasing the tangential accommodation coefficient and increases by a reduction in the normal accommodation coefficient, although the shock thickness decreased slightly for the sharpest leading edge, Kn_t of 100, as the normal accommodation coefficient changed from 1 to 0.5.

Again, the circular cylinder provides a much larger shock thickness, i.e., δ/λ_∞, of 3.35, 3.41 and 3.16 for diffuse, α_n = 0.50 and σ_t = 0.50, respectively. Compared to the flat-nose shapes, these values are about 2.0, 1.8 and 2.1 times larger than those for Kn_t of 1, respectively.

7.3. Shock Wave Shape

The shock wave shape, defined by the shock wave center location, is obtained by calculating the position that corresponds to the maximum f for class III molecules in the η-direction along the body surface (see Fig. 1(b)). The effect of incomplete surface accommodation on the shock wave shape is illustrated in Fig. 5. Figure 5(a) displays the shock wave shape for Kn_t of 100 and Fig. 5(b) for Kn_t of 1, which correspond to flat-nose bodies with thickness t/λ_∞ of 0.01 and 1, respectively. In this set of plots, X and Y are the Cartesian coordinates x and y normalized by λ_∞.
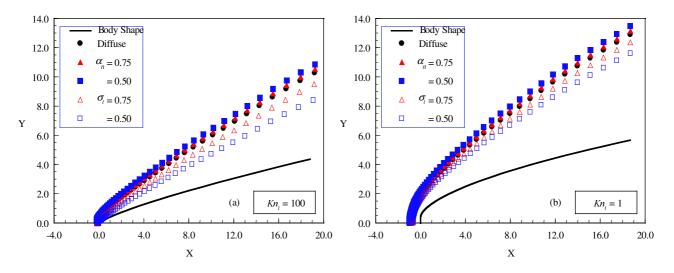

Figure 5: Shock wave shapes on flat-nose bodies as a function of the surface accommodation coefficient for leading edges that correspond to thickness Knudsen number Kn_t of (a) 100 and (b) 1.

It was pointed out by Lees and Kubota (1957) that when the freestream Mach number M_∞ is sufficiently large, the hypersonic small-disturbance equations admit similarity solutions for the asymptotic shock wave shapes over power-law bodies ($y \propto x^n$, $0 < n < 1$), where asymptotic refers to the flowfield at large distances downstream of the nose of the body. The hypersonic small-disturbance theory states that, for certain exponent n, a body defined by x^n produces a shock wave of similar shape and profiles of flow properties transverse to the stream direction that are similar at any axial station not too near the nose. At or near the nose, the surface slope, the curvature, and the higher derivatives are infinite, and the similarity solutions break down. In the more general case for $0 < n < 1$, the shock wave grows as x^m. When n grows from zero, m begins by keeping the constant value $m = 2/3$ for 2-D flow, and if n keeps on growing towards unity, m remains equal to n.

The flat-nose bodies, defined by Eq.(1), are not power-law shapes by themselves, but they can be closely fitted with power-law shapes ($\propto x^n$) far from the nose of the leading edge (Santos 2004). In this way, Fig. 6(a) displays the comparison of the flat-nose shapes and the corresponding power-law curve fit shapes. As would be expected, discrepancies have been found among the curves in the vicinity of the nose of the bodies. This behavior is brought out more clearly in Fig. 6(b), which exhibits details of the curves near the nose.

By considering the reference system located at the nose of the flat-nose bodies, $X = 0$, the fitting process, which has been performed over those bodies shown in Fig. 6, approximates the body shapes by power-law shape of the following form,

$$y = a(x + b)^n \tag{2}$$

where a is the power-law constant of the curve fit, b is the distance from the nose of the leading edge, and n is the power-law exponent of the curve fit. As a result, the body power-law exponents are 0.79, 0.72 and 0.56 for leading edges corresponding to Kn_l of 100, 10 and 1, respectively. The maximum absolute error between the original and the curve fit shapes for $X > 3$ are less than 0.12%, 0.14% and 0.30% for flat-nose thickness corresponding to Kn_l of 100, 10 and 1, respectively.
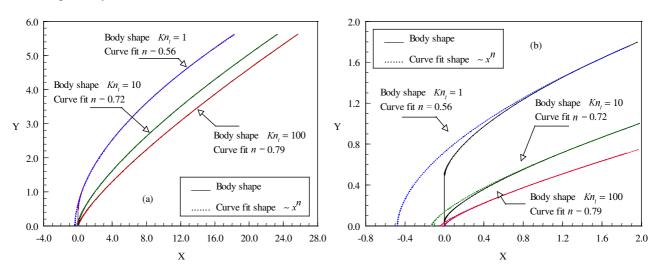

Figure 6: Comparison of flat-nose shapes with power-law curve fit shapes for leading edge thickness t/λ_∞ of 0.01, 0.1 and 1, which correspond to Knudsen number Kn_l 100, 10 and 1. (a) along the afterbody surface and (b) in the vicinity of the nose.

In what follows, the flat-nose leading edges shown in Fig. 6 are now well represented by shapes with the power-law form ($\propto x^n$) far from the nose of the leading edges. Hence, by assuming that power-law bodies generate power-law shock waves in accordance with hypersonic small-disturbance theory (Lees and Kubota, 1957), the shock location coordinates shown in Fig. 5 were used to approximate the shape of the shock wave with a curve fit. A fitting algorithm was performed over these points to approximate the shock shape as a power-law curve of the following form,

$$y = A(x + B)^m \tag{3}$$

where A is the shock wave power-law constant, B is the distance from the nose of the leading edge to the shock wave curve fit along the stagnation streamline, and m is the shock wave power law exponent.

For comparison purpose, two forms of the curve fit were considered in defining the shock shape: (1) A, B and m were found to provide the best curve fit solutions, and (2) A and B were found by keeping $m = 2/3$ for $n < 2/3$ cases, and

$m = n$ for $n \geq 2/3$ cases, where n and m stand for body and shock wave power-law exponents, respectively.

It is worthwhile mentioning that the fitting process was performed over the points yielded by DSMC simulations located far from the nose region, say $X > 3.0$, where it is expected that the blunt nose effects are not significant. It is also important to recall that the shock wave shape in the vicinity of the nose is not correctly predicted by the theoretical solutions, since the hypersonic slender body approximations are violated close to or at the nose of the leading edges as explained earlier. Moreover, the flat-nose shapes are represented by power-law shapes far from the nose region, as displayed in Fig. 6.

Curve fit solutions for shock shape over the flat-nose body with Kn_t of 100 ($t/\lambda_\infty = 0.01$), which corresponds to a body power-law exponent of 0.79, are displayed in Figs. 7(a) and 7(b) for normal and tangential accommodation coefficients of 0.5, respectively. In Fig. 7(a) (or 7(b)), the solutions given by $m = 0.798$ (or $m = 0.875$) and $m = n = 0.79$ represent, respectively, the two forms of the curve fit solutions mentioned earlier. It is apparent from this set of figures that the curve fit solutions present a good agreement, by visual inspection, with those solutions provided by the DSMC simulation. Nevertheless, as the maximum absolute error between the DSMC solutions and the curve fit solutions are calculated for coordinate points located at $X > 3.0$, it is found that the best fit is obtained for the first form of the fitting process, i.e., when A, B and m were found in order to yield the best solution. The error is less then 1.0% and 2.4% for $m = 0.798$ or 0.875 and 0.79, respectively, for the curves in Figs. 7(a) and 7(b). In general, the solutions are in qualitative agreement with the Lees and Kubota (1957) findings in the sense that the shock wave shape would follow the shape of the body for body power-law exponent $n > 2/3$.
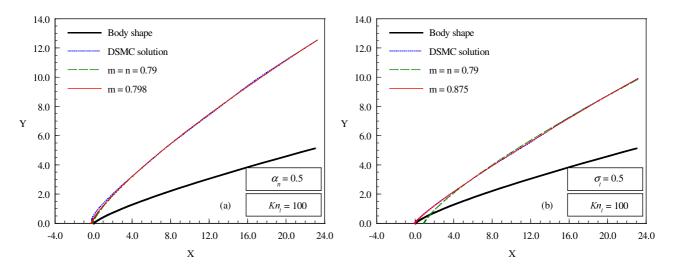

Figure 7: Shock wave shape curve fits on flat-nose body with nose thickness t/λ_∞ of 0.01, which corresponds to Knudsen number Kn_t of 100. (a) $\alpha_n = 0.5$ and (b) $\sigma_t = 0.5$.
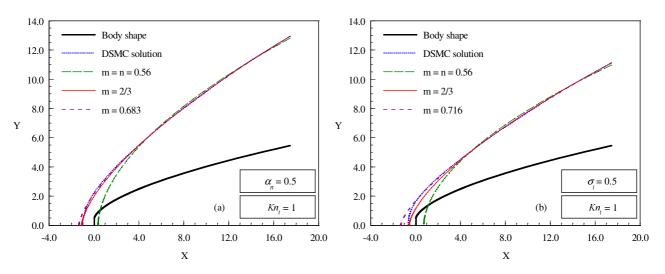

Figure 8: : Shock wave shape curve fits on flat-nose body with nose thickness t/λ_∞ of 1, which corresponds to Knudsen number Kn_t of 1. (a) $\alpha_n = 0.5$ and (b) $\sigma_t = 0.5$.

Shock shape curve fit solutions for the flat-nose body with Kn_t of 1 ($t/\lambda_\infty = 1$), which corresponds to a body power-law exponent of 0.56, are displayed in Figs. 8(a) and 8(b) for normal and tangential accommodation coefficients of 0.5, respectively. The curve fit solutions shown in this set of figures were obtained according to Eq.(3) by three different forms; in the first form, A and B were found by keeping m equal to the body shape, $m = n$; in the second form, A, B and m were found in order to obtain the best fit; finally in the third form, A and B were found by keeping m equal to 2/3, the exponent that it is expected that the shock wave would grow, according to the theory (Lees and Kubota, 1957).

Referring to Fig. 8, it is noted that the curve fit given by $m = n = 0.56$ does not match the shock wave shape obtained by the DSMC simulation, as predicted by the hypersonic small-disturbance theory (Lees and Kubota, 1957). In contrast, the two other curve fit solutions, m equal to 2/3, 0.683 in Fig. 8(a) and 0.716 in Fig. 8(b) present an excellent agreement with those solutions provided by the DSMC simulation. Once again, the curve-fitted solution deviates from the DSMC solution close to the nose of the leading edge, as would be expected.

At this point, it should be emphasized that the curve fit exponents are very sensitive to the number of coordinate points used in the fitting process, which define the shock wave center. In addition, these coordinate points present fluctuations, originated from the DSMC simulations, which were not taken into account.

8. Concluding Remarks

This study applies the Direct Simulation Monte Carlo method to investigate the shock wave structure for a family of flat-nose leading edges. The calculations have provided information concerning the nature of the shock wave detachment distance, shock wave thickness and shock wave shape resulting from variations on the thickness of the flat nose and on the surface accommodation coefficient for the idealized situation of two-dimensional hypersonic rarefied flow. The analysis also showed that the shock wave structure was affected by changes in the normal and tangential accommodation coefficients. It was found that the shock wave standoff and the shock wave thickness increased by a reduction in the normal accommodation coefficient and decreased by a reduction in the tangential accommodation coefficient for the range of the coefficient investigated. In addition, the computational results indicated that the shock wave shape grows with power-law form ($\propto x^m$), for the flat-nose bodies investigated, which can be closely fitted with power-law shapes ($\propto x^n$).

9. References

Bird, G. A., 1981, "Monte Carlo Simulation in an Engineering Context", Progress in Astronautics and Aeronautics: Rarefied gas Dynamics, Ed. Sam S. Fisher, Vol. 74, part I, AIAA New York, pp. 239-255.

Bird, G. A., 1989, "Perception of Numerical Method in Rarefied Gasdynamics", Rarefied gas Dynamics: Theoretical and Computational Techniques, Eds. E. P. Muntz, and D. P. Weaver and D. H. Capbell, Vol. 118, Progress in Astronautics and Aeronautics, AIAA, New York, pp. 374-395.

Bird, G. A., 1994, "Molecular Gas Dynamics and the Direct Simulation of Gas Flows", Oxford University Press, Oxford, England, UK.

Borgnakke, C. and Larsen, P. S., 1975, "Statistical Collision Model for Monte Carlo Simulation of Polyatomic Gas Mixture", Journal of computational Physics, Vol. 18, No. 4, pp. 405-420.

Lees, L. and Kubota, T., 1957, "Inviscid Hypersonic Flow over Blunt-Nosed Slender Bodies", Journal of Aeronautical Sciences, Vol. 24, No. 3, pp. 195-202.

Lord, R. G., 1991, "Application of the Cercignani-Lampis Scattering Kernel to Direct Simulation Monte Carlo Method", Proceedings of the 17th International Symposium on Rarefied Gas Dynamics, edited by A. E. Beylich, Aachen, Germany, pp. 1427-1433, July 8-14.

Reller Jr., J. O., 1957, "Heat Transfer to Blunt Nose Shapes with Laminar Boundary Layers at High Supersonic Speeds", NACA RM-A57FO3a.

Santos, W. F. N., 2003, "Aerodynamic Heating on Blunt Nose Shapes in Rarefied Hypersonic Flow", Proceedings of the 17th International Congress of Mechanical Engineering, COBEM 2003, 10-14 Nov, São Paulo, SP, Brazil.

Santos, W. F. N., 2004, "Numerical Prediction of Stagnation-Point Shock-Detachment Distance for Hypersonic Low-Density Flow over Blunt Nose Shapes", Proceedings of the 24th International Congress of the Aeronautical Sciences, ICAS 2004, 29 Aug – 3 Sept, Yokohama, Japan.

Santos, W. F. N., 2005, "Simulation of Round Leading Edge Aerothermodynamics", Proceedings of the 18th International Congress of Mechanical Engineering, COBEM 2005, 6-11 Nov, Ouro Preto, MG, Brazil.

Shvets, A. I., Voronin, V. I., Blankson, I. M., Khikine, V. And Thomas, L., 2005, "On Waverider Performance with Hypersonic Flight Speed and High Altitudes", 43rd AIAA Aerospace Sciences Meeting and Exhibit, AIAA Paper 2005-0512, Reno, NV.